# Orthogonal frequency-division multiplexing for simultaneous gate operations on multiple qubits via a shared control line

Haruki Mitarai<sup>®</sup>,\* Yukihiro Tadokoro<sup>®</sup>,<sup>†</sup> and Hiroya Tanaka<sup>®</sup><sup>‡</sup>
Toyota Central R&D Labs., Inc., 41-1, Yokomichi, Nagakute, Aichi 480-1192, Japan
(Dated: November 24, 2025)

The increasing number of qubits in quantum processors necessitates a corresponding increase in the number of control lines between the processor, which is typically operated at cryogenic temperatures, and external electronics. Scaling poses significant challenges in terms of the thermal loads, forming a major bottleneck in the realization of large-scale quantum computers. In this study, we analyze simultaneous gate operations on multiple qubits using microwaves transmitted via a single cable in a frequency-division multiplexing (FDM) scheme. By employing rectangular control microwave pulses, we reveal the contribution of drive frequency spacing to gate fidelity. Through theoretical and numerical analyses, we demonstrate that orthogonal and quasi-orthogonal microwave signals suppress interference in simultaneously driven qubits, thereby ensuring high gate fidelity. Additionally, we provide design guidelines for key parameters, including pulse length, number of multiplexed microwave signals, and rotation angle, to achieve precise qubit operations. Our findings enable a scalable FDM-based microwave control scheme suitable for quantum processors with a large number of qubits.

## I. INTRODUCTION

Quantum computing is expected to solve problems intractable to classical computers within realistic timescales [1]. The potential applications include prime factorization [2], quantum chemistry calculations [3–5], quantum and classical system simulations [6–9], and others [10–17]. These capabilities have attracted significant attention from both academic and industrial research communities. In recent years, substantial research and engineering efforts have been directed toward the development of fault-tolerant quantum computers [18–26]. For example, quantum supremacy and error correction using surface codes have been experimentally demonstrated using superconducting quantum processors [27, 28].

Classical control electronics are crucial for the advancement of quantum processors because they strongly affect the precision of qubit manipulation [29]. Currently, the control architectures for many types of qubits commonly generate microwave signals at ambient temperatures [30– 34. The microwave signals are then delivered to individual gubits, typically located in a dilution refrigerator, via one-to-one coaxial cabling. However, this approach faces scalability challenges for large-scale quantum computers. As the number of qubits increases, the number of required control lines increases. Typically, exploiting quantum advantages for solving realistic problems requires millions of qubits [35, 36]. Note that increasing the number of control wires not only adds hardware complexity and cost but also imposes additional heat loads through physical interconnections, thereby threatening the cooling capacity of the refrigerators [31].

Hence, wire reduction is a critical focus in scaling quantum computing systems [37–44]. Frequency-division multiplexing (FDM) is an essential technique that enables a single microwave cable to simultaneously control multiple qubits, thereby significantly reducing the number of required control lines. However, a microwave tone intended for one qubit is off-resonant for, and interferes with, other simultaneously driven qubits, thus hindering precise parallel gate operations [29, 44]. Therefore, suppressing such interference is essential to achieve high gate fidelity in the FDM scheme. Accordingly, a frequency-multiplexed qubit controller, based on adiabatic quantum-flux-parametron logic and a superconducting resonator array operating as a frequency demultiplexer, was investigated [34]. In addition, selective gate operations using pulse shaping have been demonstrated [45].

In this study, we investigate simultaneous gate operations on multiple qubits driven by a frequency-divisionmultiplexed microwave signal. We focus on the role of drive frequency spacing and its impact on gate fidelity. Through theoretical and numerical analyses, we demonstrate that orthogonal FDM (OFDM) [46–48] can mitigate interference from off-resonant microwave components owing to their orthogonality, resulting in high gate fidelity. In addition, at half the frequency spacing required for pulse orthogonality, the gate fidelity is comparable to that achieved with orthogonal spacing, even though the multiplexed microwaves are no longer mutually orthogonal. Furthermore, we discuss the design requirements for the key parameters, including pulse length, number of multiplexed microwave signals, and rotation angle, to achieve high-fidelity gate operations.

Our findings expand the design space for spectrum allocation and pulse length of microwave signals in the FDM scheme, facilitating the development of a scalable FDM-based microwave controller for quantum processors with a large number of qubits. Notably, we provide de-

<sup>\*</sup> hmitarai@mosk.tytlabs.co.jp

<sup>†</sup> y.tadokoro@ieee.org

<sup>&</sup>lt;sup>‡</sup> tanak@mosk.tytlabs.co.jp

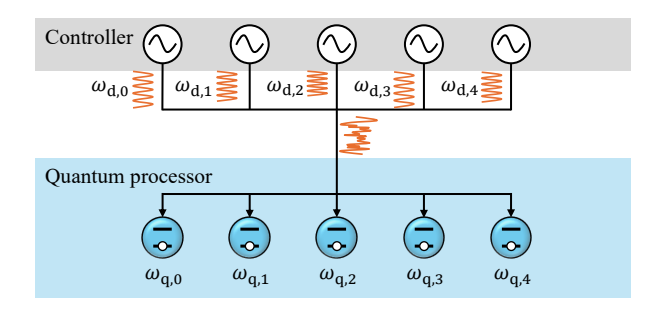


FIG. 1. Conceptual illustration of a model comprising N=5 independent qubits with frequencies  $\omega_{\mathbf{q},k}$  driven by microwaves via a shared control line. The controller produces N microwave tones at distinct frequencies  $\omega_{\mathbf{d},k}$ , which are then combined and routed to a quantum processor via the shared line. The combined signal is applied uniformly to all qubits.

sign guidelines for the FDM scheme to suppress interference and achieve high fidelity without requiring additional circuit elements. Moreover, the developed framework enables the use of closely spaced drive frequencies and short pulse lengths, thereby achieving high throughput in gate operations. Our approach is inherently scalable and well suited for controlling a large number of qubits owing to its simplicity and narrow bandwidth requirements.

### II. MODEL

Figure 1 shows a system of N independent qubits driven by a frequency-division-multiplexed microwave signal. The controller generates microwaves with N distinct frequencies that are then combined and transmitted to the quantum processor through a shared control line. The synthesized signal is applied uniformly to all the qubits. The Hamiltonian of the entire system is given by

$$H_{\text{all}}(t) \equiv \sum_{k \in K} \left[ -\frac{\omega_{\text{q},k}}{2} \sigma_{\text{z},k} + \sum_{j \in K} \alpha_{j} s\left(t\right) \sin\left(\omega_{\text{d},j} t + \theta_{j}\right) \sigma_{\text{y},k} \right], \tag{1}$$

where  $\omega_{\mathrm{d},k}$ ,  $\theta_k$ , and  $\alpha_k$  denote the frequency, phase, and amplitude, respectively, of the microwave driving the kth qubit, which has a resonance frequency  $\omega_{\mathrm{q},k}$ .  $K \subset \mathbb{Z}$  is the set of qubit indices with cardinality |K| = N. The operators  $\sigma_{\mathrm{z},k}$  and  $\sigma_{\mathrm{y},k}$  are the Pauli Z and Y operators associated with the kth qubit. The function s(t) represents the pulse envelope. Here, we set  $\hbar = 1$  for simplicity.

Since arbitrary single-qubit gates can be implemented with X and virtual-Z gates [49], we consider only the driving terms involving  $\sigma_{y,k}$ . Now, we focus on the qubit

 $k = k_0$  in Eq. (1) and analyze the system using the singlequbit Hamiltonian given by

$$H(t) \equiv -\frac{\omega_{\mathbf{q},k_0}}{2} \sigma_{\mathbf{z},k_0} + \sum_{k \in K} \alpha_k s(t) \sin(\omega_{\mathbf{d},k} t + \theta_k) \sigma_{\mathbf{y},k_0},$$
(2)

where  $k_0 \in K$  is the index of the target qubit. Equation (2) describes the dynamics of the  $k_0$ th qubit under a multiplexed microwave drive.

We then move to the frame rotating at the qubit frequency  $\omega_{\mathbf{q},k_0}$ . Let  $|\psi_{\mathbf{I}}(t)\rangle \equiv e^{iH_0t} |\psi(t)\rangle$  be the state vector in the rotating frame, where  $H_0 \equiv -\frac{\omega_{\mathbf{q},k_0}}{2}\sigma_{\mathbf{z},k_0}$  and  $|\psi(t)\rangle$  denotes the state vector in the laboratory frame. The time evolution of the system is described by the Schrödinger equation in the frame rotating at  $\omega_{\mathbf{q},k_0}$ :  $i|\psi_{\mathbf{I}}\rangle = H_{\mathbf{I}}|\psi_{\mathbf{I}}\rangle$ , where

$$H_{\rm I}(t) = \frac{1}{2} s(t)$$

$$\sum_{k \in K} \alpha_k \left[ \sigma_{{\rm x},k_0} \left\{ \cos \left( \left( \omega_{{\rm d},k} + \omega_{{\rm q},k_0} \right) t \right) - \cos \left( \left( \omega_{{\rm d},k} - \omega_{{\rm q},k_0} \right) t \right) \right\} + \sigma_{{\rm y},k_0} \left\{ \sin \left( \left( \omega_{{\rm d},k} + \omega_{{\rm q},k_0} \right) t \right) + \sin \left( \left( \omega_{{\rm d},k} - \omega_{{\rm q},k_0} \right) t \right) \right\} \right]. \tag{3}$$

Here,  $\sigma_{\mathbf{x},k}$  represents the Pauli X operator associated with the kth qubit. For simplicity, we assume  $\theta_k = 0$  throughout this paper.

We assume that the microwave pulses have rectangular envelopes. Additionally, we set  $\omega_{\mathbf{q},k} = \omega_{\mathbf{d},k}$  for all  $k \in K$ , and allocate  $\omega_{\mathbf{q},k}$  (and  $\omega_{\mathbf{d},k}$ ) at regular intervals  $\Delta \ll \omega_{\mathbf{q},k}, \omega_{\mathbf{d},k}$ . We apply the same gate operation to all the qubits simultaneously. Therefore, we set  $\alpha_k = \alpha$  for all k. Under these assumptions, the system Hamiltonian  $H_{\mathbf{I}}$  in Eq. (3) is expressed as

$$H_{\rm I}(t) = \frac{\alpha}{2} s(t)$$

$$\sum_{k \in K} \left[ \sigma_{{\rm x},k_0} \left\{ \cos \left( (2\omega_{{\rm q},k_0} + \Delta_{kk_0}) t \right) - \cos \left( \Delta_{kk_0} t \right) \right\} + \sigma_{{\rm y},k_0} \left\{ \sin \left( (2\omega_{{\rm q},k_0} + \Delta_{kk_0}) t \right) + \sin \left( \Delta_{kk_0} t \right) \right\} \right],$$
(4)

where  $\Delta_{kj} \equiv (k-j)\Delta$ ,

$$s(t) = \begin{cases} 1 & 0 \le t \le \tau \\ 0 & \text{otherwise} \end{cases}$$
 (5)

and  $\tau$  is the pulse length. In this context, the qubit index set K is given by  $K=\{k\in\mathbb{Z}\,|\,l\leq k\leq r\},$  where r-l+1=N.

## III. GENERAL ANALYSIS

In FDM-based systems, the microwave component driving a specific qubit interferes with the operation of other qubits. Hence, suppressing the interference from the off-resonant microwave components is crucial. To quantify the interference from off-resonant microwaves, we use the average gate fidelity  $F(U_1, U_2)$ , defined as [50]

$$F(U_1, U_2) \equiv \frac{\left| \operatorname{Tr} \left( U_1^{\dagger} U_2 \right) \right|^2 + d}{d(d+1)}, \tag{6}$$

where  $U_1$  and  $U_2$  are unitary operators and d is the dimension of the Hilbert space. Ideally, quantum computers should have high average gate fidelity  $F\left(U_{\text{ideal}},U\right)$  while simultaneously realizing closely spaced drive frequencies or short pulse lengths. In the remainder of this paper,  $U_{\text{ideal}} \equiv e^{i\frac{\phi}{2}\sigma_{\mathbf{x},k_0}}$  denotes the desired unitary operator on a two-dimensional Hilbert space with the rotation angle  $\phi$ . The operator U is defined as  $|\psi_{\mathbf{I}}\left(\tau\right)\rangle = U\left|\psi_{\mathbf{I}}\left(0\right)\right\rangle$ .

We employ the second-order Magnus expansion [51] to approximate the evolution of the state  $|\psi_{\rm I}\rangle$ . We define the approximate evolution operator  $U_{\rm Magnus}$  as

$$U_{\text{Magnus}}(t) \equiv \exp\left[-i\left\{\Omega_1(t) + \Omega_2(t)\right\}\right], \tag{7}$$

where

$$\Omega_1(t) \equiv \int_0^t H_{\rm I}(t_1) \,\mathrm{d}t_1,\tag{8}$$

$$\Omega_2(t) \equiv -\frac{i}{2} \int_0^t \int_0^{t_1} \left[ H_{\rm I}(t_1), H_{\rm I}(t_2) \right] dt_2 dt_1.$$
 (9)

To obtain the closed-form expressions for Eqs. (8) and (9), we approximate  $H_{\rm I}$  as

$$H_{\rm I}(t) \sim \frac{\alpha}{2} s(t)$$

$$\sum_{k \in K} \left[ -\sigma_{\mathrm{x},k_0} \cos\left(\Delta_{kk_0} t\right) + \sigma_{\mathrm{y},k_0} \sin\left(\Delta_{kk_0} t\right) \right], \quad (10)$$

by neglecting the fast oscillating terms in Eq. (4). Substituting Eq. (10) instead of Eq. (4) into Eq. (8), we obtain

$$\Omega_1(\tau) \sim -(\sigma_{\mathbf{x},k_0}\lambda_{\mathbf{x}} + \sigma_{\mathbf{y},k_0}\lambda_{\mathbf{y}}),$$
 (11)

where

$$\lambda_{\mathbf{x}} \equiv \frac{\alpha \tau}{2} \left[ 1 + \sum_{\substack{k \in K \\ k \neq k_0}} \operatorname{sinc}(\Delta_{kk_0} \tau) \right], \tag{12}$$

$$\lambda_{\rm y} \equiv -\frac{\alpha \tau}{2} \sum_{k \in \gamma} \sin\left(\frac{\Delta_{kk_0} \tau}{2}\right) \operatorname{sinc}\left(\frac{\Delta_{kk_0} \tau}{2}\right),$$
 (13)

by using  $\operatorname{sinc}(x) \equiv \operatorname{sin}(x)/x$ . Here,  $\gamma \subset K$  is the set of qubit indices that lack corresponding elements related to  $k_0$  (see Fig. 2).

Substituting Eq. (10) into Eq. (9), we obtain

$$\Omega_2(\tau) \sim -\sigma_{\mathbf{z},k_0} \lambda_{\mathbf{z}},$$
 (14)

where

$$\lambda_{\mathbf{z}} \equiv \frac{\alpha^{2}\tau}{4} \left[ \sum_{k \in \gamma} \frac{\cos(\Delta_{kk_{0}}\tau) - \frac{3}{2}\mathrm{sinc}(\Delta_{kk_{0}}\tau)}{\Delta_{kk_{0}}} + \sum_{k \in \gamma} \sum_{\substack{j \in K \\ j \neq k_{0}}} \left\{ \frac{\mathrm{sinc}\left(\Delta_{jk_{0}}\tau\right)}{\Delta_{kk_{0}}} + \frac{\mathrm{sinc}\left[\left(\Delta_{kk_{0}} + \Delta_{jk_{0}}\right)\tau\right]}{2\Delta_{jk_{0}}} \right\} - \sum_{k \in K} \sum_{\substack{j \in K \\ j \neq k_{0}}} \frac{\mathrm{sinc}\left[\left(\Delta_{kk_{0}} + \Delta_{jk_{0}}\right)\tau\right]}{2\Delta_{jk_{0}}} - \sum_{k \in \gamma} \sum_{\substack{j \in K \\ j \neq k_{0} \\ j \neq k}} \left\{ \frac{1}{\Delta_{kk_{0}}} + \frac{1}{\Delta_{jk_{0}}} \right\} \frac{\mathrm{sinc}(\Delta_{kj}\tau)}{2} \right].$$
 (15)

Inserting Eqs. (11) and (14) into Eq. (7), we obtain

 $U_{\mathrm{Magnus}}\left(\tau\right)$ 

$$\sim \mathbb{I}\cos\left(\Lambda\right) + i\frac{1}{\Lambda}\left(\lambda_{x}\sigma_{x,k_{0}} + \lambda_{y}\sigma_{y,k_{0}} + \lambda_{z}\sigma_{z,k_{0}}\right)\sin\left(\Lambda\right),\tag{16}$$

where

$$\Lambda \equiv \sqrt{\lambda_{\rm x}^2 + \lambda_{\rm y}^2 + \lambda_{\rm z}^2},\tag{17}$$

and I is the identity operator. From Eq. (16), the average

gate fidelity  $F\left(U_{\text{ideal}}, U_{\text{Magnus}}\left(\tau\right)\right)$  can be expressed as

$$F\left(U_{\text{ideal}}, U_{\text{Magnus}}\left(\tau\right)\right) \sim \frac{1}{3} \left(2 \left|\cos\left|\frac{\phi}{2}\right| \cos\Lambda + \frac{\phi\lambda_{x}}{|\phi|\Lambda} \sin\left|\frac{\phi}{2}\right| \sin\Lambda\right|^{2} + 1\right). \tag{18}$$

Equation (18) indicates that high fidelity,  $F\left(U_{\text{ideal}}, U_{\text{Magnus}}\left(\tau\right)\right) \sim 1$ , can be attained in regimes where  $\lambda_{\text{x}} \sim \phi/2$  and  $\lambda_{\text{y}}, \lambda_{\text{z}} \sim 0$ .

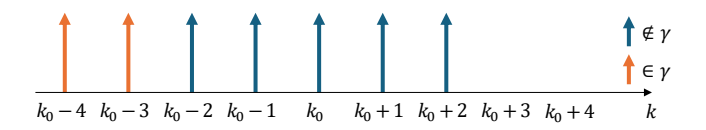


FIG. 2. Illustration of  $\gamma$ , which represents the set of qubit indices lacking a corresponding element with respect to  $k_0$ . The orange and blue arrows denote the driving microwaves that correspond and do not correspond to the set  $\gamma$ , respectively. In this figure, the set  $\gamma$  is specifically  $\{k_0-3,k_0-4\}$ . These indices have no counterpart related to  $k_0$ , i.e., there are no arrows at  $k_0+3$  and  $k_0+4$ .

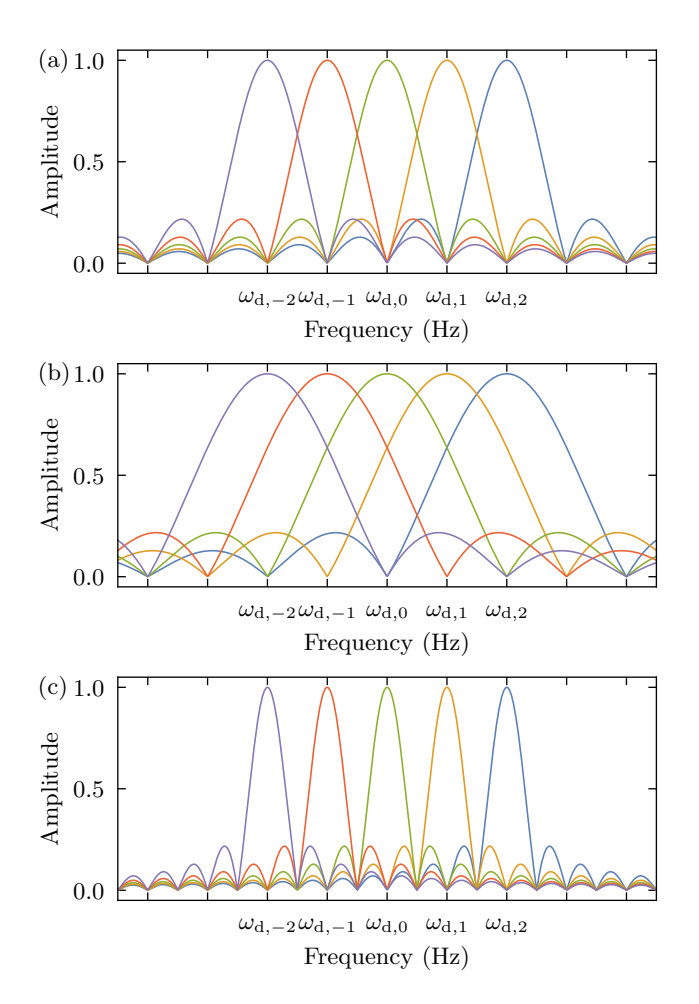


FIG. 3. Absolute values of the spectra of  $s(t)\sin(\omega_{\mathrm{d},k}t)$  for N=5 and  $k\in\{-2,-1,0,1,2\}$ , with pulse length (a)  $\tau=\tau_0$ , (b)  $\tau=\tau_0/2$ , and (c)  $\tau=2\tau_0$ . In (a) and (c), each drive frequency  $\omega_{\mathrm{d},k}$  is placed at the zero-crossing point of the spectral components of all other microwaves.

### IV. CASE STUDIES

Here, we demonstrate that high fidelity can be obtained for several specific pulse length values  $\tau$ . Specifically, we analyze cases in which  $\tau = \tau_0$  (Sec. IV A),

 $\tau = \tau_0/2$  (Sec. IV B), and  $\tau \gg \tau_0$  as the long-pulse limit (Sec. IV C), where  $\tau_0 \equiv 2\pi/\Delta$ .

Note that a larger frequency spacing  $\Delta$  mitigates the influence of the off-resonant drive. A shorter pulse length  $\tau$  corresponds to a wider spectral width, requiring a larger  $\Delta$  to attain high fidelity; conversely, reducing  $\Delta$  requires increasing  $\tau$ . In this sense, minimizing  $\tau$  for a fixed  $\Delta$  is essentially equivalent to minimizing  $\Delta$  for a fixed  $\tau$ ; both increase the gate operation throughput (i.e., the number of gates executable per unit time) within a given total bandwidth. For a practical implementation,  $\tau$  can be adjusted by tuning the microwave controller, which is generally a more straightforward method than manipulating  $\Delta$ . Therefore, in the remainder of this paper, we focus on identifying the pulse lengths that yield higher fidelity values rather than varying  $\Delta$ .

## A. Orthogonal case $(\tau = \tau_0)$

We consider  $\tau=\tau_0$ , where the microwave signals are mutually orthogonal. That is, the peak of the frequency spectrum of one microwave signal aligns with the null points of the spectra of all the other microwave signals, as illustrated in Fig. 3(a). Such a spectrum allocation is commonly used in wireless communication systems and is known as OFDM, enabling subcarrier signals to overlap in the frequency domain without causing interference [46–48]. Therefore, it is anticipated that high gate fidelity can be achieved when  $\tau=\tau_0$ .

Notably, because  $\sin(n\Delta\tau_0) = 0$  and  $\sin(n\frac{\Delta\tau_0}{2}) = 0$  for all integers n, Eqs. (12), (13), and (15) reduce to

$$\lambda_{\mathbf{x}} = \frac{\phi}{2},\tag{19}$$

$$\lambda_{y} = 0, \tag{20}$$

$$\lambda_{\mathbf{z}} = \frac{\phi^2}{8\pi} \sum_{k \in \gamma} \frac{1}{k - k_0},\tag{21}$$

when  $\alpha = \phi/\tau$ . This reduction suggests that the interference from off-resonant microwaves is suppressed, thereby achieving high gate fidelity. In fact, we observe that  $F\left(U_{\text{ideal}}, U_{\text{Magnus}}(\tau)\right) \sim 1$  near  $k_0 = 0$  at  $\tau = \tau_0$ , as shown in Fig. 4(a). Here,  $F\left(U_{\text{ideal}}, U_{\text{Magnus}}(\tau)\right)$  is calculated using Eqs. (18) and (19)–(21) for N=15, -l=r=7, and  $\phi=\pi/2$ . This result indicates that orthogonal drive frequencies provide high gate fidelity.

Note that the fidelity degrades as  $|k_0|$  increases. This degradation is attributed to the corresponding increase in  $|\lambda_z|$ , which conflicts with the condition for high fidelity, which requires  $\lambda_z$  to be zero [see Fig. 5(a)].

## B. Quasi-orthogonal case $(\tau = \tau_0/2)$

Next, we examine the case where  $\tau = \tau_0/2$ , which is half the duration required for pulse orthogonality, and illustrate the spectra of the microwave signals in Fig. 3(b).

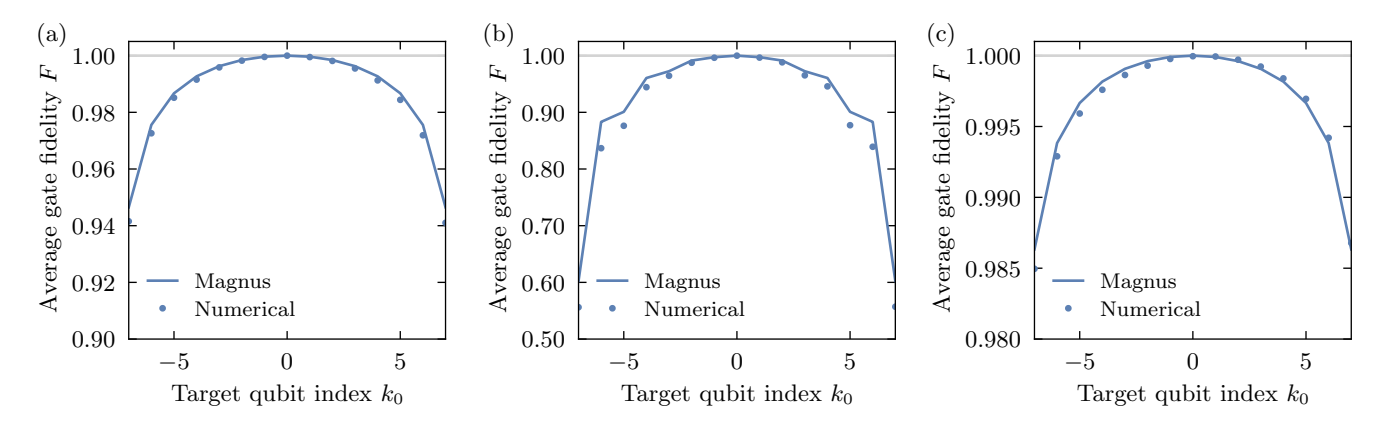


FIG. 4. Average gate fidelity  $F\left(U_{\text{ideal}}, U_{\text{Magnus}}(\tau)\right)$  (solid lines) and  $F\left(U_{\text{ideal}}, U\right)$  (dots) as a function of the target qubit index  $k_0$ , for three pulse lengths: (a)  $\tau = \tau_0$ , (b)  $\tau = \tau_0/2$ , and (c)  $\tau = 2\tau_0$ . Parameters are set as N = 15, -l = r = 7,  $\omega_{q,k_0}/2\pi = 5 \,\text{GHz}$ ,  $\Delta/2\pi = 10 \,\text{MHz}$ ,  $\phi = \pi/2$ , and  $\alpha = \phi/\tau$ .

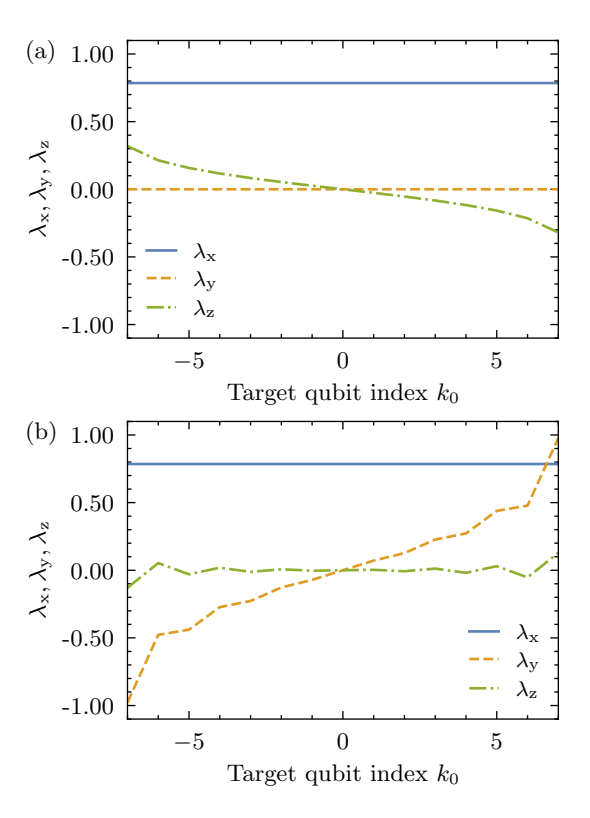


FIG. 5. Rotation angles  $\lambda_{\rm x}$ ,  $\lambda_{\rm y}$ , and  $\lambda_{\rm z}$  as a function of the target qubit index  $k_0$  for (a) orthogonal ( $\tau = \tau_0$ ) and (b) quasi-orthogonal ( $\tau = \tau_0/2$ ) cases. Parameters are set as N = 15, -l = r = 7, and  $\phi = \pi/2$ . Results are obtained using Eqs. (19)–(21) for (a) and Eqs. (22)–(24) for (b).

In this case, the microwaves are no longer mutually orthogonal. Equations (12), (13), and (15) are rewritten as

follows:

$$\lambda_{\mathbf{x}} = \frac{\phi}{2},\tag{22}$$

$$\lambda_{y} = \frac{\phi}{2\pi} \sum_{k \in \gamma} \frac{(-1)^{k-k_0} - 1}{k - k_0},$$
 (23)

$$\lambda_{\mathbf{z}} = \frac{\phi^2}{4\pi} \sum_{k \in \gamma} \frac{(-1)^{k-k_0}}{k - k_0},\tag{24}$$

when  $\alpha = \phi/\tau$ . Using Eqs. (18) and (22)–(24),  $F(U_{\text{ideal}}, U_{\text{Magnus}}(\tau))$  is plotted as a function of  $k_0$  in Fig. 4(b). The same parameters as those used in Fig. 4(a) are used, except for pulse length  $\tau$ . Interestingly, the average gate fidelity for  $\tau = \tau_0/2$  [Fig. 4(b)] is qualitatively similar to that for  $\tau = \tau_0$  [Fig. 4(a)] around  $k_0 = 0$ . In other words, the system exhibits high gate fidelity.

However, an increase in  $|k_0|$  leads to a larger degradation in the gate fidelity than in the case where  $\tau=\tau_0$ . This degradation arises from the difference in the behavior of  $\lambda_{\rm y}$  and  $\lambda_{\rm z}$  between  $\tau=\tau_0/2$  and  $\tau=\tau_0$ , as shown in Fig. 5(b). The value of  $|\lambda_{\rm y}|$  increases with  $|k_0|$  [dashed line in Fig. 5(b)] at  $\tau=\tau_0/2$ , which is a significant factor in fidelity reduction. In contrast, at  $\tau=\tau_0$ , an increase in  $|\lambda_{\rm z}|$  [dash-dotted line in Fig. 5(a)] contributes to a reduction in fidelity. The magnitude of  $\lambda_{\rm y}$  for  $\tau=\tau_0/2$  is clearly larger than that of  $\lambda_{\rm z}$  for  $\tau=\tau_0$ , resulting in smaller gate fidelity when  $\tau=\tau_0/2$ .

## C. Long-pulse limit $(\tau \gg \tau_0)$

Finally, we present the results for  $\tau \gg \tau_0$ , where a longer pulse length corresponds to a narrower spectral width of the drive pulse. Considering the orthogonal microwaves  $\tau = m\tau_0$ , where m is a positive integer,

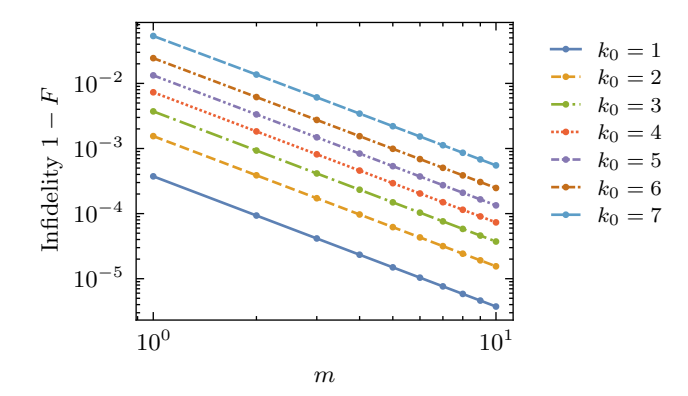


FIG. 6. Infidelity  $1 - F\left(U_{\text{ideal}}, U_{\text{Magnus}}(\tau)\right)$  as a function of the integer  $m = \tau/\tau_0$ . The parameters are N = 15, -l = r = 7,  $\phi = \pi/2$ , and  $\alpha = \phi/\tau$ . Since the infidelity shows similar behavior for  $k_0 = \pm k$  (where k is a positive integer) and the infidelity becomes zero for  $k_0 = 0$ , the results for  $k_0 \leq 0$  are omitted here.

Eqs. (12), (13), and (15) can be simplified as follows:

$$\lambda_{\mathbf{x}} = \frac{\phi}{2},\tag{25}$$

$$\lambda_{y} = 0, \tag{26}$$

$$\lambda_{\mathbf{z}} = \frac{\phi^2}{8\pi m} \sum_{k \in \gamma} \frac{1}{k - k_0},\tag{27}$$

when  $\alpha = \phi/\tau$ . We now focus on  $\tau = 2\tau_0$ , which corresponds to the spectra shown in Fig. 3(c). Figure 4(c) shows the gate fidelity  $F(U_{\text{ideal}}, U_{\text{Magnus}}(\tau))$  calculated using Eqs. (18) and (25)–(27). The fidelity is higher than that for  $\tau = \tau_0$  [Fig. 4(a)] and  $\tau = \tau_0/2$  [Fig. 4(b)] for the entire range of  $k_0$ .

Moreover, using Eqs. (25)–(27), we plot the infidelity  $1-F\left(U_{\rm ideal},U_{\rm Magnus}\left(\tau\right)\right)$  as a function of the integer  $m=\tau/\tau_0$  in Fig. 6, employing the same parameters as those used in Fig. 4. Notably,  $1-F\left(U_{\rm ideal},U_{\rm Magnus}\left(\tau\right)\right)$  fits well to linear functions on a log-log scale with slopes of approximately -2.0. This indicates that the infidelity  $1-F\left(U_{\rm ideal},U_{\rm Magnus}\left(\tau\right)\right)$  decreases proportionally to  $\tau^{-2}$  when  $\tau=m\tau_0$ .

We now turn to the long-pulse limit  $\tau \to \infty$ , without restricting  $\tau$  to  $m\tau_0$ . Assuming  $\alpha = \phi/\tau$  and constant  $\Delta$ , Eqs. (12), (13), and (15) become

$$\lambda_{\rm x} \to \frac{\phi}{2},$$
 (28)

$$\lambda_{\rm y} \to 0,$$
 (29)

$$\lambda_{\rm z} \to 0.$$
 (30)

Hence, we obtain

$$U_{\text{Magnus}}(\tau) \to e^{i\frac{\phi}{2}\sigma_{\mathbf{x},k_0}} = U_{\text{ideal}},$$
 (31)

and therefore,

$$F\left(U_{\text{ideal}}, U_{\text{Magnus}}\left(\tau\right)\right) \to 1.$$
 (32)

Thus, higher gate fidelity can be achieved with a longer pulse length. This result is consistent with our intuition, that is, longer pulse lengths correspond to less interference.

#### D. Discussion

The pulse length is a crucial factor for enabling dense spacing of drive frequencies while maintaining high gate fidelity. From the results presented in Secs. IV A and IV B, we observe that high fidelity can be attained near  $k_0=0$  at both  $\tau=\tau_0$  and  $\tau=\tau_0/2$ . This is because the rotation angles are  $\lambda_{\rm x}\sim\phi/2$  and  $\lambda_{\rm y},\lambda_{\rm z}\sim0$  in each case, which is necessary to achieve high fidelity. An equivalent result can be obtained for every integer multiple of  $\tau_0$  and  $\tau_0/2$ . Consequently, we conclude that  $\tau$  should be chosen from the set  $\{m\tau_0/2\}$ , where m is a positive integer, to obtain higher fidelity around  $k_0=0$ . In addition, a larger  $\tau$  guarantees high fidelity because the rotation angles approach  $\lambda_{\rm x}\to\phi/2$  and  $\lambda_{\rm y},\lambda_{\rm z}\to0$  in the limit of infinite pulse duration  $(\tau\to\infty)$ , as shown in Sec. IV C.

However, the nonzero  $\lambda_{\rm y}$  and  $\lambda_{\rm z}$  degrade the average gate fidelity when  $|k_0|$  increases. For example, when  $\tau=\tau_0$  (Sec. IV A),  $\lambda_{\rm x}=\phi/2$  and  $\lambda_{\rm y}=0$  are satisfied. However,  $\lambda_{\rm z}$  causes a reduction in fidelity. A closer examination reveals that  $\lambda_{\rm z}$  becomes zero when the second- and higher-order terms such as  $\Omega_2\left(\tau\right)$  are neglected in the Magnus expansion. The absence of higher-order terms underlies the OFDM scheme in wireless communication systems [46–48], where the subcarrier frequencies are closely spaced while orthogonality is maintained, thereby avoiding intercarrier interference. In contrast, quantum dynamics introduce additional complexity in the context of qubit control. In particular, contributions from the noncommutativity of the time-dependent Hamiltonian become significant.

Finally, we plot numerical results  $[F(U_{ideal}, U)]$  using the dots in Figs. 4(a)–4(c). The unitary operator U is calculated by numerically solving the Schrödinger equation using Eq. (2). Consequently, the theoretical results are consistent with the numerical analysis, thereby validating the approximations underlying our theoretical analysis.

## V. PARAMETER STUDIES

Here, we numerically investigate the relationship between the fidelity  $F(U_{\text{ideal}}, U)$  and the key parameters: pulse length  $\tau$  (Sec. VA), number of control microwave signals N, corresponding to the number of qubits (Sec. VB), and rotation angle  $\phi$  (Sec. VC). The time evolution of the system is obtained numerically by simulating the Schrödinger equation using the Hamiltonian given by Eq. (2).

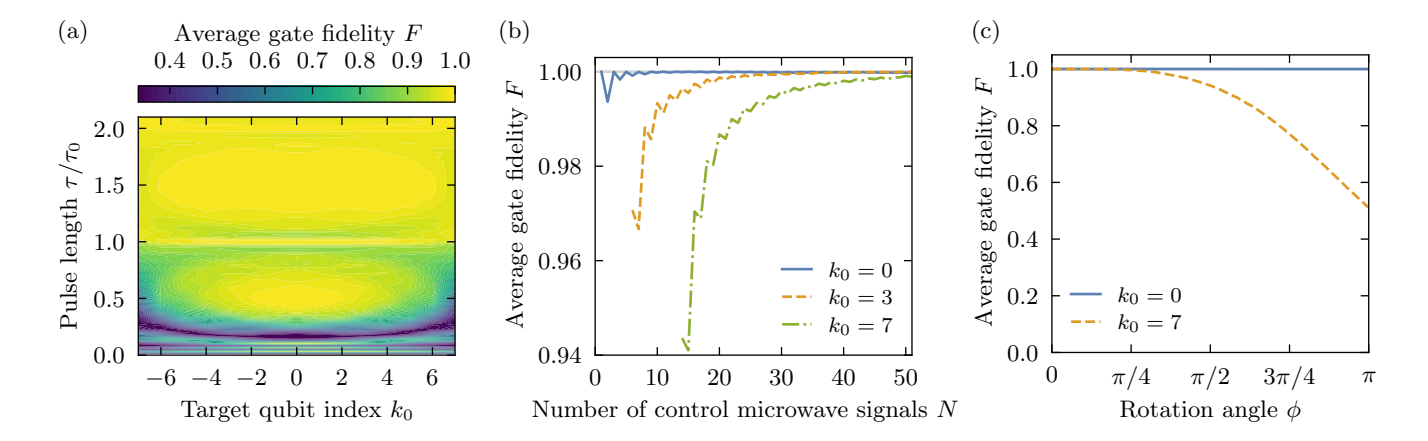


FIG. 7. Average gate fidelity  $F\left(U_{\text{ideal}},U\right)$  as a function of (a) target qubit index  $k_0$  and pulse length  $\tau$ , (b) number of control microwave signals N, and (c) rotation angle  $\phi$ . Common parameters for (a)–(c) are  $\omega_{q,0}/2\pi = 5\,\text{GHz}$ ,  $\Delta/2\pi = 10\,\text{MHz}$ , and  $\alpha = \phi/\tau$ . The other parameters are (a) N = 15, -l = r = 7, and  $\phi = \pi/2$ ; (b)  $l = -\lfloor (N-1)/2 \rfloor$ ,  $r = \lfloor N/2 \rfloor$ ,  $\phi = \pi/2$ , and  $\tau = \tau_0$ ; and (c) N = 15, -l = r = 7, and  $\tau = \tau_0$ . In (b), the fidelity is not shown in N < 6 for  $k_0 = 3$  and in N < 14 for  $k_0 = 7$ , since the drive microwave components for those qubits do not exist in those regimes.

#### A. Pulse length $\tau$

We analyze the dependence of the average gate fidelity on the pulse length  $\tau$  and target qubit index  $k_0$  to identify suitable pulse lengths that yield high gate fidelity. Note again that a change in  $\tau$  is equivalent to a change in  $\Delta$  as described in Sec. IV. Figure 7(a) shows a map of  $F(U_{\rm ideal}, U)$  for N=15 qubits. Throughout the entire region  $\tau/\tau_0 > 1$ , the fidelity is close to unity because a large  $\tau/\tau_0$  corresponds to a narrow lobe width of the spectrum and mitigates the interference from the off-resonant drive. In addition, at  $\tau/\tau_0 = 1$ , mutually orthogonal microwave signals provide locally maximized fidelity. Even at  $\tau/\tau_0 = 0.5$ , the fidelity exhibits a local maximum. These results are consistent with the theoretical results presented in Sec. IV.

### B. Number of control microwave signals N

We investigate the relationship between the average gate fidelity  $F(U_{\text{ideal}}, U)$  and the number of control microwave signals N corresponding to the number of qubits. Figure 7(b) shows  $F(U_{\text{ideal}}, U)$  as a function of N for  $\tau = \tau_0$ . An increase in N leads to higher fidelity. The effect of increasing N becomes more pronounced as  $k_0$  increases. This observed fidelity enhancement is achieved by the deliberate incorporation of suitably chosen off-resonant frequency components into the control pulse. This finding challenges the conventional view that off-resonant microwave components are merely detrimental to qubit control. Therefore, our results align with the emerging understanding of recent research, exemplified by methods such as active leakage cancellation demonstrated in transmon qubits [52].

Notably, the fidelity curves exhibit a jagged structure.

This behavior arises from the asymmetry in the frequency allocation of the control microwave signals:  $F(U_{\text{ideal}}, U)$  for an operation on the qubit with frequency  $\omega_{d,k_0}$  tends to be higher when the microwave frequencies are symmetrically allocated around it.

#### C. Rotation angle $\phi$

In addition to  $\tau$  and N, the rotation angle  $\phi \propto \alpha$  associated with each pulse is a key parameter for the gate operations. Figure 7(c) shows the average gate fidelity  $F\left(U_{\text{ideal}},U\right)$  as a function of  $\phi$  for  $N=15,\,\tau=\tau_0$ , and  $\alpha=\phi/\tau$ . We plot the fidelity for two different target qubit indices:  $k_0=0$  and  $k_0=7$ . For  $k_0=0$ , high fidelity is maintained over the entire range of  $0\leq\phi\leq\pi$ . However, for  $k_0=7$ , the fidelity decreases rapidly as  $\phi$  increases. Therefore, a small rotation angle  $\phi$  (or equivalently a small  $\alpha$ ) is recommended for high-fidelity gate operations.

## VI. CONCLUSION

We have analyzed an FDM-based qubit control scheme that does not require additional circuit elements. We have focused on the pulse length, equivalently considering the spacing of the drive frequencies, to achieve high-fidelity simultaneous gate operations on multiple qubits through a single control line. Our results indicate that orthogonality of the drive-pulse frequencies considerably improves gate fidelity. Notably, even when the frequency spacing was reduced to half of the orthogonal condition, the system retained comparable fidelity levels. These results potentially broaden the design space for spectrum allocation and pulse length of microwave signals.

Our approach shares conceptual similarities with OFDM, a technique widely used in wireless communication systems. However, unlike OFDM in wireless communication systems, the noncommutativity of the time-dependent Hamiltonian in quantum systems introduces residual crosstalk. Addressing such quantum effects to further enhance the gate fidelity is an important direction for future research.

As a final remark, we have neglected leakage to higher energy levels, which can limit gate fidelity in weakly anharmonic systems such as transmons. This simplification allows us to isolate and clarify the essential physics of the OFDM scheme. A full treatment of multilevel dynamics including nonadiabatic transitions is beyond the present scope and will be addressed in future work.

#### ACKNOWLEDGMENTS

This study used QuTiP [53] for numerical calculations.

- M. A. Nielsen and I. L. Chuang, Quantum computation and quantum information (Cambridge University Press, 2010).
- [2] P. W. Shor, Polynomial-time algorithms for prime factorization and discrete logarithms on a quantum computer, SIAM Rev. 41, 303 (1999).
- [3] A. Kandala, A. Mezzacapo, K. Temme, M. Takita, M. Brink, J. M. Chow, and J. M. Gambetta, Hardwareefficient variational quantum eigensolver for small molecules and quantum magnets, Nature 549, 242 (2017).
- [4] Google AI Quantum and Collaborators, Hartree-Fock on a superconducting qubit quantum computer, Science **369**, 1084 (2020).
- [5] H. Takahashi, T. Tomaru, T. Hirano, S. Tahara, and F. Sato, Chemical reaction simulator on quantum computers by first quantization (II)—basic treatment: Implementation, J. Chem. Theory Comput. 20, 9290 (2024).
- [6] S. Lloyd, Universal quantum simulators, Science 273, 1073 (1996).
- [7] Y. Kim, A. Eddins, S. Anand, K. X. Wei, E. Van Den Berg, S. Rosenblatt, H. Nayfeh, Y. Wu, M. Zaletel, K. Temme, and A. Kandala, Evidence for the utility of quantum computing before fault tolerance, Nature 618, 500 (2023).
- [8] P. C. S. Costa, S. Jordan, and A. Ostrander, Quantum algorithm for simulating the wave equation, Phys. Rev. A 99, 012323 (2019).
- [9] Y. Sato, H. Tezuka, R. Kondo, and N. Yamamoto, Quantum algorithm for partial differential equations of non-conservative systems with spatially varying parameters, Phys. Rev. Appl. 23, 014063 (2025).
- [10] L. K. Grover, A fast quantum mechanical algorithm for database search, in *Proceedings of the Twenty-Eighth An*nual ACM Symposium on Theory of Computing, STOC '96 (Association for Computing Machinery, New York, NY, USA, 1996) pp. 212–219.
- [11] A. W. Harrow, A. Hassidim, and S. Lloyd, Quantum algorithm for linear systems of equations, Phys. Rev. Lett. 103, 150502 (2009).
- [12] A. Peruzzo, J. McClean, P. Shadbolt, M.-H. Yung, X.-Q. Zhou, P. J. Love, A. Aspuru-Guzik, and J. L. O'Brien, A variational eigenvalue solver on a photonic quantum processor, Nat. Commun. 5, 4213 (2014).
- [13] E. Farhi, J. Goldstone, and S. Gutmann, A quantum approximate optimization algorithm, arXiv:1411.4028 (2014).
- [14] P. Rebentrost, M. Mohseni, and S. Lloyd, Quantum sup-

- port vector machine for big data classification, Phys. Rev. Lett. **113**, 130503 (2014).
- [15] K. Mitarai, M. Negoro, M. Kitagawa, and K. Fujii, Quantum circuit learning, Phys. Rev. A 98, 032309 (2018).
- [16] S. Gao, F. Hayes, S. Croke, C. Messenger, and J. Veitch, Quantum algorithm for gravitational-wave matched filtering, Phys. Rev. Res. 4, 023006 (2022).
- [17] N. Ishida and Y. Hasegawa, Quantum-computer-based verification of quantum thermodynamic uncertainty relation, Phys. Rev. E 112, 034124 (2025).
- [18] Y. Nakamura, Y. A. Pashkin, and J. S. Tsai, Coherent control of macroscopic quantum states in a single-Cooper-pair box, Nature 398, 786 (1999).
- [19] A. Blais, R.-S. Huang, A. Wallraff, S. M. Girvin, and R. J. Schoelkopf, Cavity quantum electrodynamics for superconducting electrical circuits: An architecture for quantum computation, Phys. Rev. A 69, 062320 (2004).
- [20] J. Koch, T. M. Yu, J. Gambetta, A. A. Houck, D. I. Schuster, J. Majer, A. Blais, M. H. Devoret, S. M. Girvin, and R. J. Schoelkopf, Charge-insensitive qubit design derived from the Cooper pair box, Phys. Rev. A 76, 042319 (2007).
- [21] L. DiCarlo, J. M. Chow, J. M. Gambetta, L. S. Bishop, B. R. Johnson, D. I. Schuster, J. Majer, A. Blais, L. Frunzio, S. M. Girvin, and R. J. Schoelkopf, Demonstration of two-qubit algorithms with a superconducting quantum processor, Nature 460, 240 (2009).
- [22] M. Steffen, D. P. DiVincenzo, J. M. Chow, T. N. Theis, and M. B. Ketchen, Quantum computing: An IBM perspective, IBM J. Res. Dev. 55, 13:1 (2011).
- [23] Y. Zhao, Y. Ye, H.-L. Huang, Y. Zhang, D. Wu, H. Guan, Q. Zhu, Z. Wei, T. He, S. Cao, F. Chen, T.-H. Chung, H. Deng, D. Fan, M. Gong, et al., Realization of an errorcorrecting surface code with superconducting qubits, Phys. Rev. Lett. 129, 030501 (2022).
- [24] D. Bluvstein, S. J. Evered, A. A. Geim, S. H. Li, H. Zhou, T. Manovitz, S. Ebadi, M. Cain, M. Kalinowski, D. Hangleiter, J. P. Bonilla Ataides, N. Maskara, I. Cong, X. Gao, P. Sales Rodriguez, et al., Logical quantum processor based on reconfigurable atom arrays, Nature 626, 58 (2024).
- [25] A. Anferov, S. P. Harvey, F. Wan, J. Simon, and D. I. Schuster, Superconducting qubits above 20 GHz operating over 200 mK, PRX Quantum 5, 030347 (2024).
- [26] S. Konno, W. Asavanant, F. Hanamura, H. Nagayoshi, K. Fukui, A. Sakaguchi, R. Ide, F. China, M. Yabuno, S. Miki, H. Terai, K. Takase, M. Endo, P. Marek, R. Filip, et al., Logical states for fault-tolerant quantum compu-

- tation with propagating light, Science 383, 289 (2024).
- [27] F. Arute, K. Arya, R. Babbush, D. Bacon, J. C. Bardin, R. Barends, R. Biswas, S. Boixo, F. G. S. L. Brandao, D. A. Buell, B. Burkett, Y. Chen, Z. Chen, B. Chiaro, R. Collins, et al., Quantum supremacy using a programmable superconducting processor, Nature 574, 505 (2019).
- [28] Google Quantum AI and Collaborators, Quantum error correction below the surface code threshold, Nature 638, 920 (2025).
- [29] J. P. G. van Dijk, E. Kawakami, R. N. Schouten, M. Veldhorst, L. M. K. Vandersypen, M. Babaie, E. Charbon, and F. Sebastiano, Impact of classical control electronics on qubit fidelity, Phys. Rev. Appl. 12, 044054 (2019).
- [30] J. M. Hornibrook, J. I. Colless, I. D. Conway Lamb, S. J. Pauka, H. Lu, A. C. Gossard, J. D. Watson, G. C. Gardner, S. Fallahi, M. J. Manfra, and D. J. Reilly, Cryogenic control architecture for large-scale quantum computing, Phys. Rev. Appl. 3, 024010 (2015).
- [31] S. Krinner, S. Storz, P. Kurpiers, P. Magnard, J. Heinsoo, R. Keller, J. Lüetolf, C. Eichler, and A. Wallraff, Engineering cryogenic setups for 100-qubit scale superconducting circuit systems, EPJ Quantum Technol. 6, 2 (2019).
- [32] J. P. G. van Dijk, E. Charbon, and F. Sebastiano, The electronic interface for quantum processors, Microprocess. Microsyst. 66, 90 (2019).
- [33] X. Xue, B. Patra, J. P. G. van Dijk, N. Samkharadze, S. Subramanian, A. Corna, B. Paquelet Wuetz, C. Jeon, F. Sheikh, E. Juarez-Hernandez, B. P. Esparza, H. Rampurawala, B. Carlton, S. Ravikumar, C. Nieva, et al., CMOS-based cryogenic control of silicon quantum circuits, Nature 593, 205 (2021).
- [34] N. Takeuchi, T. Yamae, T. Yamashita, T. Yamamoto, and N. Yoshikawa, Microwave-multiplexed qubit controller using adiabatic superconductor logic, npj Quantum Inf. 10, 53 (2024).
- [35] A. G. Fowler, M. Mariantoni, J. M. Martinis, and A. N. Cleland, Surface codes: Towards practical large-scale quantum computation, Phys. Rev. A 86, 032324 (2012).
- [36] D. Litinski, A game of surface codes: Large-scale quantum computing with lattice surgery, Quantum 3, 128 (2019).
- [37] J. C. Bardin, E. Jeffrey, E. Lucero, T. Huang, S. Das, D. T. Sank, O. Naaman, A. E. Megrant, R. Barends, T. White, M. Giustina, K. J. Satzinger, K. Arya, P. Roushan, B. Chiaro, et al., Design and characterization of a 28-nm bulk-CMOS cryogenic quantum controller dissipating less than 2 mW at 3 K, IEEE J. Solid-State Circuits 54, 3043 (2019).
- [38] J. P. G. Van Dijk, B. Patra, S. Subramanian, X. Xue, N. Samkharadze, A. Corna, C. Jeon, F. Sheikh, E. Juarez-Hernandez, B. P. Esparza, H. Rampurawala, B. R. Carlton, S. Ravikumar, C. Nieva, S. Kim, et al., A scalable cryo-CMOS controller for the wideband frequency-multiplexed control of spin qubits and transmons, IEEE J. Solid-State Circuits 55, 2930 (2020).

- [39] R. Huang, X. Geng, X. Wu, G. Dai, L. Yang, J. Liu, and W. Chen, Cryogenic multiplexing control chip for a superconducting quantum processor, Phys. Rev. Appl. 18, 064046 (2022).
- [40] S. Chakraborty, D. J. Frank, K. Tien, P. Rosno, M. Yeck, J. A. Glick, R. Robertazzi, R. Richetta, J. F. Bulzacchelli, D. Underwood, D. Ramirez, D. Yilma, A. Davies, R. V. Joshi, S. D. Chambers, et al., A cryo-CMOS lowpower semi-autonomous transmon qubit state controller in 14-nm FinFET technology, IEEE J. Solid-State Circuits 57, 3258 (2022).
- [41] P. Zhao, R. Wang, M.-J. Hu, T. Ma, P. Xu, Y. Jin, and H. Yu, Baseband control of superconducting qubits with shared microwave drives, Phys. Rev. Appl. 19, 054050 (2023).
- [42] N. Takeuchi, T. Yamae, W. Luo, F. Hirayama, T. Yamamoto, and N. Yoshikawa, Scalable flux controllers using adiabatic superconductor logic for quantum processors, Phys. Rev. Res. 5, 013145 (2023).
- [43] H. Shen, N. Takeuchi, Y. Yamanashi, and N. Yoshikawa, Amplitude-controllable microwave pulse generator using single-flux-quantum pulse pairs for qubit control, Supercond. Sci. Technol. 36, 095010 (2023).
- [44] R. Ohira, R. Matsuda, H. Shiomi, K. Ogawa, and M. Negoro, Optimizing multi-tone microwave pulses via phase selection for quantum computing applications, J. Appl. Phys. 136, 114402 (2024).
- [45] R. Matsuda, R. Ohira, T. Sumida, H. Shiomi, A. Machino, S. Morisaka, K. Koike, T. Miyoshi, Y. Kurimoto, Y. Sugita, Y. Ito, Y. Suzuki, P. A. Spring, S. Wang, S. Tamate, et al., Selective excitation of superconducting qubits with a shared control line through pulse shaping, arXiv:2501.10710 (2025).
- [46] R. W. Chang, Synthesis of band-limited orthogonal signals for multichannel data transmission, Bell Labs Tech. J. 45, 1775 (1966).
- [47] T. Hwang, C. Yang, G. Wu, S. Li, and G. Ye Li, OFDM and its wireless applications: A survey, IEEE Trans. Veh. Technol. 58, 1673 (2009).
- [48] J. G. Andrews, S. Buzzi, W. Choi, S. V. Hanly, A. Lozano, A. C. K. Soong, and J. C. Zhang, What will 5G be?, IEEE J. Sel. Areas Commun. 32, 1065 (2014).
- [49] D. C. McKay, C. J. Wood, S. Sheldon, J. M. Chow, and J. M. Gambetta, Efficient Z gates for quantum computing, Phys. Rev. A 96, 022330 (2017).
- [50] L. H. Pedersen, N. M. Møller, and K. Mølmer, Fidelity of quantum operations, Phys. Lett. A 367, 47 (2007).
- [51] W. Magnus, On the exponential solution of differential equations for a linear operator, Commun. Pure Appl. Math. 7, 649 (1954).
- [52] B. Chiaro and Y. Zhang, Active leakage cancellation in single qubit gates, Phys. Rev. Lett. 135, 130601 (2025).
- [53] N. Lambert, E. Giguère, P. Menczel, B. Li, P. Hopf, G. Suárez, M. Gali, J. Lishman, R. Gadhvi, R. Agarwal, A. Galicia, N. Shammah, P. Nation, J. R. Johansson, S. Ahmed, et al., QuTiP 5: The quantum toolbox in Python, arXiv:2412.04705 (2024).